Gaped Two-Loop Antenna-Based Magnetic Transceiver With an Empirical Model for Wireless Underground Communication

JAEWOO LEE[ID]**, HYUN JOON LEE, JANG-YEOL KIM**[ID]**, AND IN-KUI CHO**[ID]

Radio and Satellite Research Division, Electronics and Telecommunications Research Institute, Daejeon 34129, South Korea

Corresponding author: Jaewoo Lee (jaewoo@etri.re.kr)

ABSTRACT This paper presents a practical low-power, low-frequency magnetic induction (MI) transceiver based on symmetrical gaped two-loop antennas with an empirical circuit model for wireless underground communication. Because of the quasi-two-dimensional loop antennas for the transmitter (Tx) and the receiver (Rx), the tailored hardware platform is not only simple, but can be readily extended to a mutually orthogonal 3-D scheme. Through a mixed model of actual measurement data and theoretical parameters, we developed the two-loop antenna with the space of the antenna radius optimized for energy efficiency. The Tx power almost doubles that of the single Tx one, which provides channel expansion as well as system stability in terms of the Tx current level. Accordingly, the Rx signal is considerably increased by 9.5 dB in contrast with a typical single-Tx single-Rx configuration. Moreover, we used empirical-based modeling for a reliable electrical model. The empirical mutual inductance, which was modeled in a 25 m corridor, resulted in a channel correction factor of 0.86, showing that the signal intensity was reduced by 14% in the underground corridor compared to the free space. A maximum range of 68 m under a SNR of 9.5 dB and a path loss of 100.7 dB on a load of 50 Ω at 34.5 dBm were predicted from the model. In addition, this study confirmed the system feasibility by a SNR of 8.7 dB in a practical lossy environment between two floors, where its value was converted into a MI channel at a distance of 70 m in the underground corridor.

INDEX TERMS Magnetic fields, electromagnetic induction, electronic circuits, modeling, wireless communication.

I. INTRODUCTION

Wireless Internet of Things (IoT) platforms are applied to a specific environment by means of cutting-edge technology to monitor and control infrastructure in limited or inaccessible circumstances. Wireless underground sensor networks (WUSNs) based on classical electromagnetic (EM)-wave technology in an air medium, e.g., Bluetooth or ZigBee [1]–[3], are effective owing to their high-data rates [1], low-cost competitiveness [2], and low-power consumption [3]. However, unlike normal or steady state systems, these EM wave systems cannot operate if the propagation path is blocked by solid materials with high absorption of EM waves. For the mmWave bands, EM waves

The associate editor coordinating the review of this manuscript and approving it for publication was Jie Tang[ID].

deteriorate rapidly in solid channels due to the skin effect [4], [5]. For harsh environments, using a very low frequency (VLF, 3 kHz to 30 kHz) band with a wavelength of 10 km or more, can be a solution [5], [6]. However, conventional transceivers of the WUSNs in the VLF band may suffer from large dipole antenna sizes [6]. Additionally, two-way wireless communication or localization is necessary to connect and rescue people who are suddenly trapped without power in a building or mine collapse. Then, a battery-powered mobile platform at the physical layer of the WUSNs is essential for the underground emergency response [7], [8].

Many magnetic induction (MI)-based communication systems have been found in the literature for underground [4], [5], [7]–[10] and underwater [11]–[13] applications. In particular, low-frequency two MI link systems, MI communication [5]–[7], [9], [10], [14]–[16] and MI

localization [2], [8], [17]–[21], comprise a promising method in extreme underground environments for rescue apparatuses for two-way connection. The two applications are divided into the physical layer and the data link/node networking [6]–[8]. Here, their physical layer is generally similar for the case of an emergency disaster, so the hardware design requirement is limited to the MI-based link system. The hardware design of WUSNs leads to the crucial factors [6]: the antenna volume, the operating frequency, the transmitter (Tx) power, and the receiver (Rx) readout module. Firstly, two-way communication requires a small antenna scheme with wavelength independence, and configurations are implemented in the two types: the narrow band resonant type (high efficiency) or the wideband flat coil type (low efficiency) [3]–[5]. The resonant type is mainly used due to power efficiency. The resonant loop antenna induces a magnetic field directly related to the data at an operating frequency that depends only on the matching capacitance, not the diameter of the loop antenna [3], [4]. This feature allows a loop antenna to be small and makes the mobile MI-link feasible [2], [8], [15], [16]. Secondly, the fundamental necessity to readily connect between underground channels is the operating frequency [5], [8], [14]. The operation frequency can strongly affect both the bandwidth of the system and the skin depth [4]–[8] of the magnetic channel. The higher the operating frequency is, the larger the bandwidth is with respect to the hardware system design, but this also reduces the skin depth. The long-wavelength (VLF) band or near (2 kHz or 125 kHz) can penetrate solid media, such as rock, aqueous soil, concrete, air, or wood, etc., in the condition of the quasi-static field (the reactive near field) rather than the propagation wave (the far field) causing multipath loss or fading influence [5]–[8], [11], [16]. For this reason, the operating frequency that satisfies the skin depth must be selected. For example, the skin depth at the VLF band is in the range of 29 m to 92 m when the conductivity of complex media is assumed as 0.01 S/m. Thirdly, when the above two conditions are satisfied, the Tx power range determines the ability of bidirectional communication [2], [3], [8]. Regarding the feasibility of mobile sensor nodes, low-power small transceivers benefit from the loop antenna scheme. Here, the magnetic intensity decreases rapidly with an increasing distance (path loss of 60 dB/decade) [8], because the magnetic intensity is inversely proportional to the cube of the distance between two coupled antennas in the near field [2]. Given the low operation frequency, the coverage within tens of meters is subsequently controlled by the transmitter (Tx) power (more than 30 dBm). In [2], the MI-based WSNs were presented using a commercial off-the-shelf (COTS) product. However, it is not simple to control the output power or the minimum received signal (80 μV) [2] due to the COTS system. Thus, dealing with tailored Tx power is important to enhance the overall performance. Lastly, the receiver (Rx) features, such as the signal-to-noise ratio (SNR), path loss (*PL*), and magnetic flux density [6], [8] etc., can be characterized from the magnetic medium and the Tx power along with the Rx

readout module (Rx-RM). The signal integrity of Rx antennas is improved by the deployment configuration of a MI guided scheme [4], [17] or multi-loop coils [7], [19]. The lifetime of a mobile sensor node is determined by the budget of the power management. For example, at a 5 V (USB 3.0 voltage) bias, a 10,000 mAh rechargeable battery (Xiaomi, PLM13ZM, 37 Wh) can continuously handle a 37 dBm Tx module for 7.4 hours.

An equivalent circuit model [2]–[4], [9]–[11], [14], [15] reflecting practical boundary conditions is necessary to design a MI data link system. This model has the advantage of properly predicting the performance of the entire hardware system, including solid media. However, some parameters cannot be obtained by theoretical models. For a real environment, it seems complicated or not easy to estimate the mutual inductance [3], [4], [17] in terms of the connectivity between the Tx and the Rx. In [4], the mutual inductance was modeled by the theoretical equation, but the deviation in real circumstances is not negligible (in our case: 14% for the Tx part). The modeled mutual inductance is too simplified as an ideal assumption. Moreover, the evaluation of the Tx parasitic resistance related to the Tx power level is impossible by theoretical calculation due to a practical characteristic. The Tx parasitic resistance of a closed loop circuit can only be extracted from empirical data to determine the proper Tx power. If this parameter is not clear, it should be omitted [3], [4], [17]. In this case, the circuit model tends to be simplified with limited reliability. For example, the ratio of the parasitic to intrinsic resistance in our Tx electrical circuit is 60%, which shows that the parasitic resistance has to be defined and evaluated. Thus, when modeling equivalent circuits, empirical variables in the real world must be considered in order to accurately design the performance of the hardware system.

In this paper, we provide a detailed description of a symmetrical gaped two-loop antenna-based low-frequency MI transceiver with an empirical circuit model in order to realize the hardware system of WUSNs for practical two-way underground connectivity, and we investigate its feasibility in real underground environments (two-story space). We focus only on issues related to the node design (magnetic field formation, degree of influence of magnetic channel, magnetic field sensing), leaving the network/node networking to the system designer [6]. The features and contributions are listed as follows.

- We give a practical low-power MI transceiver based on symmetrical gaped two-loop antennas for WUSNs, which is applicable to two-way communication as the hardware system of a mobile sensor node.
- We devise a highly efficient quasi 2-D antenna block. Since this antenna module can be readily extended to a mutually orthogonal 3-D scheme [2], [3], [21], it can be used as a core antenna block for various applications of WUSNs
- We provide an empirical circuit model for each module (Tx, Rx) including a practical magnetic channel, and

evaluate the performance of the whole system using the model. This reliable model helps one intuitive to understand the MI link system.

· We realize whether a MI-based link system could be used in buildings with concrete walls, and show the preliminary data as a reference. Conveniently, researchers can design and implement MI-based link systems from many given key parameters.

The outline of the paper is as follows. Section II briefly describes the theoretical background of both MI between two coils and the proposed MI transceiver. Section III discusses the Tx part while Section IV presents the Rx part for detecting signals in a MI based channel. Section V describes the proposed MI-based link system and its equivalent circuit. Section VI discusses several channel effects involving underground environments. The paper is concluded in Section VII.

II. LOW FREQUENCY MI LINK SYSTEM

This section explains the MI principle of a coupled loop antenna and describes a MI-based link system for underground applications. The MI theoretical background is presented by the structure of two coupled circular loop antennas. Each Tx and Rx characteristic is analyzed into four cases. Through this comparison, we introduce the proposed MI transceiver.

A. MI OPERATION PRINCIPLES

When a loop coil is operating in a band much lower than the self-resonant frequency, it can be approximated by a series-connected circuit with a resistor and an inductor [3], [4], [9]–[11]. If two loop coils are deployed at some interval d_{ch}, they are coupled by mutual inductance M_{ch}, changing to the equivalent impedance for each other. As one of the two loop coils with radius a_t and a_r, respectively, is applied to the Tx part with a signal current i_t as shown in Fig. 1, the signal from i_t is detected in the other as the Rx part at distance d_{ch} on the basis of Biot–Savart's law. Here, P is a point located on the Rx coil with angle θ_t relative to the Z axis in a cartesian coordinate system. The magnetic vector potential $A_t(\phi)$ at P with regard to the Tx coil is given by [3], [4]

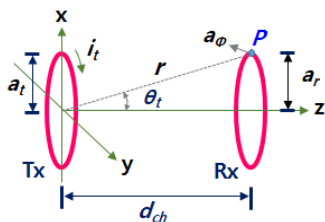$$A_t(\phi) = \frac{\mu_0 i_t \pi a_t^2 a_r}{4(d_{ch}^2 + a_r^2)^{3/2}} a_\phi \qquad (1)$$

FIGURE 1. Detailed illustration of a mutual inductance between two circular coils: orientation, coil scheme, and coupling principle.

where μ_0 is the space permeability. The magnetic flux is given by integrating $A_t(\phi)$ around the Rx coil with a_r. M_{ch} is obtained from the magnetic flux at the Rx coil divided by i_t. Since M_{ch} for each other is symmetrical, it is given by [3], [4], [11]

$$M_{ch} = \frac{\mu_0 \pi N_t N_r a_t^2 a_r^2}{2(d_{ch}^2 + a_r^2)^{3/2}} \qquad (2)$$

where N_t and N_r are the number of coil turns on each side. Thus, increasing the radius of both coils to the upper limit is more effective than raising N_t and N_r under $d_{ch} \gg a_r$ conditions [3], [4]. For two-way MI connectivity, we chose the maximum radius of two coupled antennas to 0.25 m.

For an intuitive understanding, we selected four cases from a variety of loop coil configurations and compared them, as shown in Fig. 2. It is noted that all of the four cases as a core antenna block can be extended or applied to a mutually-orthogonal effective 3-D antenna scheme. The first case is the simplest way: the conventional configuration for one Tx and one Rx (Case 1: single-Tx single-Rx) as seen in Fig. 2(a). It communicates through two coupled coils at d_{ch}. Case 2 is a method of adding a coil at the Rx part in Case 1. If two identical Rx coils with one Tx coil (Case 2: single-Tx two-Rx) are applied at the conditions of $d_{ch} \gg a_t$, the induced voltage V_{ch} in the Rx part can be doubled due to the two Rx coils, as shown in Fig. 2(b). At a given Tx power, it can be effective without a large Tx power loss; for instance, in our case, we needed an additional Tx power of at least 3 dBm to double the induced voltage at a distance of 25 m. Conversely, Case 3 is an inverse combination of Case 2. Fig. 2(c) is a method of Case 3 (two-Tx single-Rx) extending the transmission distance almost twice compared to Case 1. This structure is suitable for broadcasting systems between large base stations and small sensor nodes. Case 4 is a structure that improves both Tx and Rx characteristics. In order to simultaneously extend the coverage and improve the sensitivity of the Rx part, Case 2 should be combined
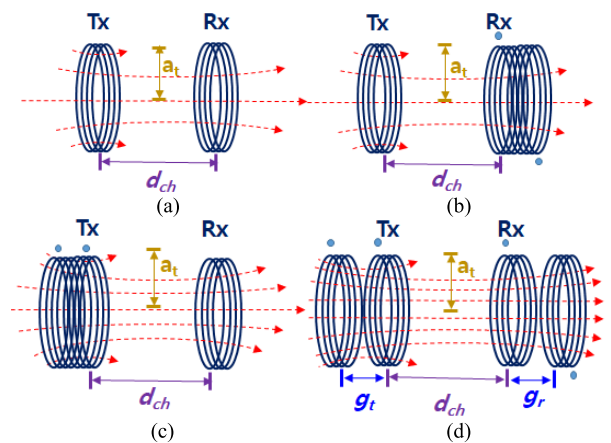

FIGURE 2. Loop antenna configuration of (a) single-Tx single-Rx (Case 1) (b) single-Tx two-Rx (Case 2) (c) two-Tx single-Rx (Case 3) (d) gaped two-Tx gaped two-Rx (Case 4).
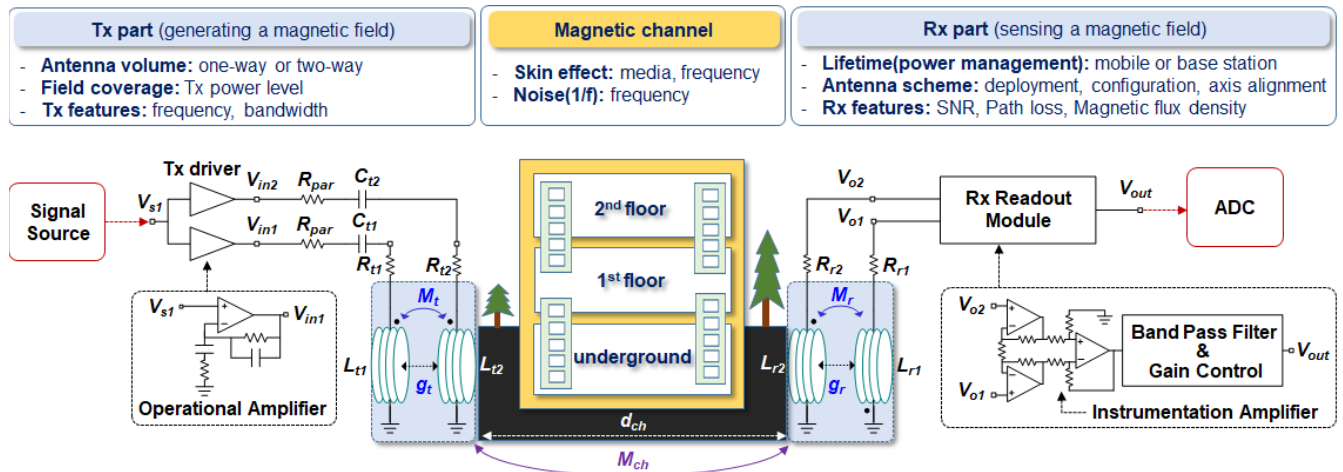
FIGURE 3. Schematic concept for the proposed MI link system based on gaped two-loop antennas for WUSNs through a practical underground circumstance.

with Case 3, which creates Case 4 (gaped two-Tx gaped two-Rx) as shown in Fig. 2(d). Here, an important factor is M_{ch}. The tight coupling between the two coils interferes with the two coils' current flow. Obviously, some spacing g_t and g_r between them on both sides can be adjusted for both high Tx power and an enhanced received signal. Thus, Fig. 2(d) shows the optimized scheme.

B. GAPED TWO-LOOP ANTENNA-BASED MI SYSTEM

Fig. 3 shows a proposed MI transceiver based on gaped two-loop antennas, which is divided into three parts: the Tx module (magnetic field formation), the magnetic channel (degree of influence of magnetic channel), and the Rx module (magnetic field sensing) [3], [4], [6]–[8]. Each item considered for design in the three areas of the physical layer is also shown. The design of the Tx module is related to an antenna volume and field coverage as well as the operation frequency and the bandwidth, while the issues of the Rx module are a transceiver lifetime, an antenna scheme, and Tx characteristics. Here, all the variables will be investigated except for the lifetime issue which is mainly the domain of the networking design. Also, for the magnetic channel, both the skin depth [5] and the background noise [8] are dorminantly working as a design parameter. The skin depth works as the parameter of the upper limitation for the operation frequency, whereas the background noise is considered as the bottom limitation. We chose the lowest frequency band (19 kHz - 21 kHz) of the International Telecommunication Union-Radio communication Sector/Study Groups 1 (ITU-R/SG1) standard dealing with wireless power transmission compatible with loop antenna and its driver.

The Tx module consists of four blocks: two Tx drivers with input voltage V_{s1} and output voltages V_{in1}, V_{in2} from a signal source, series resistors R_{t1}, R_{t2} and series inductors L_{t1}, L_{t2} consisting of a loop antenna, matching capacitors C_{t1}, C_{t2} controlling an operating frequency, and parasitic

resistance R_{par} in a closed electrical circuit. The Rx module is composed of two loop antennas, which are symmetrical to the Tx part and an Rx-RM. Like the Tx part, the two antennas are consisting of series resistors R_{r1}, R_{r2} and series inductors L_{r1}, L_{r2}. The Rx-RM detects and amplifies two tiny input signals to an analog-to-digital converter (ADC). The magnetic channel of MI-based RF link system is linked by M_{ch} of symmetrical antennas at d_{ch}. The Tx module is usually relevant to a Tx power, whereas the Rx module are related to V_{ch} (or sensitivity). The magnetic channel is mostly associated with path loss *PL*. For the underwater case [11], 40 dBm is required because of the inverse proportion of the field intensity to the cubic of the distance. It is noted that Joule heating can degrade the system. This means that the transmission distance and the system stability are at odds. Therefore, the design of Tx power plays an important role in determining the performance of the overall system.

In turn, we chose two loop coils at an interval (Case 4), which not only improved the Tx power, but also mitigated the negative effects of M_{ch}, while maintaining the stability of the system. The parallel structure equally shared the total current. The two coils for the two sides were considered to be equally effective coils because d_{ch} was much wider than the spacing between two adjacent coils g_t or g_r. In addition, to simplify the entire link system, the antenna of the Rx part was designed with the same structure (Case 4) as the Tx part, which produced a symmetrical scheme. Moreover, the Rx-RM was developed to effectively improve the sensitivity from the instrumentation amplifier.

III. TRANSMITTING SYSTEM

This section describes a high Tx power system for MI-based RF links. A Tx module based on Case 4 is equipped with a Tx driver. Characterization of the Tx driver is first done to design the Tx power. In addition, the antenna for Case 4 is analyzed for electrical and mechanical models. As mentioned in the

previous section, it is designed for the class of about 40 dBm power to implement mobile two-way communication.

A. Tx DRIVER AND GAPED TWO-LOOP ANTENNAS

Prior to developing the quasi 2-D antenna, a Tx driver is modeled to estimate the Tx power, especially for the impedance of the signal source R_{in} and R_{par}. In [2]–[4], [17], the equivalent model was oversimplified by omitting R_{in} and R_{par} even though the magnitude was not negligible for R_{in} or not predictable for R_{par} due to empirical data. Thus, we modeled the equivalent circuit on the basis of empirical parameters. The Tx driver was chosen for the BJT-based differential amplifier where negative feedback was applied to control the gain and frequency response. The theoretical power conversion efficiency of the push-pull amplifier for Class-AB is 78.5 % due to a single power supply, but the output characteristics were degraded by many aggregation factors of lumped elements. The open voltage gain of the driver was 51.5 dBV. The output stage was composed of the Dalington structure where Q_1 was an NPN-type transistor (BC817), Q_2 was an NPN-type power transistor (MJD31), Q_3 was a PNP-type transistor (BC807), Q_4 was a PNP-type power transistor (MJD32), as shown in Fig. 4(a). The current gain was determined to be 26,000 from Q_2's current gain β_2 of 130 multiplied by Q_1's current gain β_1 of 200. If the Tx current I_t was 2.38 A, the output impedance $2R_{in}$ was equal to $r_{e1}/(\beta_2 + 1) + r_{e2} = 1.38\Omega/131 + 10.5$ mΩ = 21 mΩ. Using the negative feedback, the frequency response is determined as follows:

$$\frac{V_{n1}(j\omega)}{V_{s1}(j\omega)} \approx \frac{1 + j\omega R_{d2}C_{d1}}{(1 + j\omega R_{d1}C_{d1})(1 + j\omega R_{d2}C_{d2})} \quad (3)$$
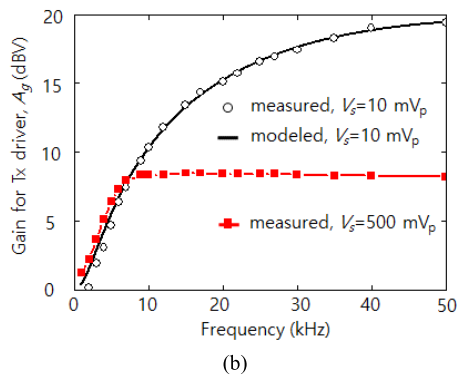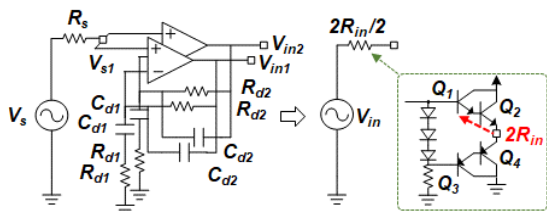
where R_{d1}, R_{d2}, C_{d1}, C_{d2} were 1 kΩ, 14 kΩ, 3.3 nF, 47 pF, respectively. The simulated and measured data are shown in Fig. 4(b). With (3), the theoretical dominant zero was 3.45 kHz whereas the two poles were 48.25 kHz and 241.3 kHz, respectively. As a result, we tailored the output signal under 10 kHz with C_{d1} of 3.3 nF rather than 33 nF to control the background noise. The measured data agreed well with the simulation data. Fig. 5 shows the implemented Tx driver module on the printed circuit board (PCB).

For a high Tx power, we developed a small loop antenna with a radius of 0.25 m and 17 turns as shown in Fig. 6. Here, the diameter of each turn was 3 mm consisting of 700 strains of 40 AWG litz wire. Theoretically, the self-inductance of a circular coil can be determined as $\mu_0 \pi N_t^2 a_t/2$ [4], [9], [10]. However, the ideal assumption may deviate from the practical litz wire-based coils. Thus, we chose an empirical method to rearrange the initial number of turns as an effective number of turns N_{e-t}, showing that N_{e-t} is 23.29 from the LCR meter. In accordance with the correction factor α_a, the modeled L_{t1} was determined as $\mu_0 \pi (\alpha_a N_t)^2 a_t/2$, where α_a was 1.37. At 20.84 kHz, L_{t1} and R_{t1} were 268 μH and 0.5 Ω, respectively. As with L_{t1}, it was also difficult to model the mutual inductance from the theoretical mutual inductance M_{t-the} on account of the complex boundary conditions. Thus, the empirical mutual inductance $M_t (= \alpha_t M_{t-the})$ was adopted, where α_a was the correction factor of Tx. A loop antenna with C_{t1} had the first resonant frequency at $(2\pi f_{res})^2 = 1/L_{t1}C_{t1}$. If one coil with C_{t1} was coupled to
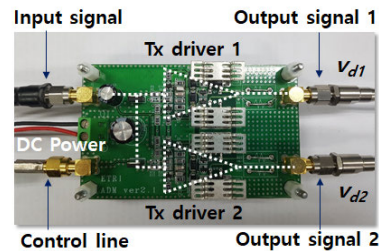

(a)

(b)

FIGURE 4. (a) Two Tx drivers connected with a signal source and equivalent circuit representation (b) measured and modeled gain performances for a Tx driver.

FIGURE 5. Fabricated Tx driver module with two output terminals through the PCB with lumped elements.
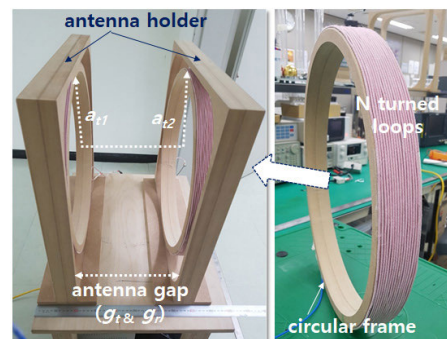

FIGURE 6. Two circular loop antennas with an interval composed of N turned-litz wire on wood circular frames.

the identical one in parallel, M_t could be extracted from the measured f_{res} due to the coupling influence

B. IMPLEMENTATION FOR THE TX MODULE

The equivalent circuit of a Tx module for Case 4 was modeled as shown in Fig. 7(a). The KVL equations are given as

$$V_{in} = (R_{t1-tot} + j\omega L_{t1} + 1/j\omega C_{t1})I_1 + j\omega M_t I_2 \quad (4a)$$

$$V_{in} = j\omega M_t I_1 + (R_{t2-tot} + j\omega L_{t2} + 1/j\omega C_{t2})I_2 \quad (4b)$$

where $R_{t1-tot} = 2R_{in}+2R_{par}+R_{t1}$, $R_{t2-tot} = 2R_{in}+2R_{par}+R_{t2}$, I_1 and I_2 are the currents for the two Tx coils, and I_t is the Tx current. As I_1 is equal to I_2 and $I_t = I_1 + I_2$, $Z_{e-t} = V_{in}/2I_1 = R_{in} + R_{par} + R_{e-t} + j\omega L_{e-t} + 1/j\omega C_{e-t}$ where $R_{e-t} = R_{t1}/2$, $L_{e-t} = [L_{t1} + M_t(g_t)]/2$ and $C_{e-t} = 2C_{t1}$. R_{par} is determined from a measured loop current as well as R_{in} and R_{t1} when V_{in} of a Tx driver is measured at a given V_s in Fig. 4(b). Also, from the series resonant condition, $M_t(g_t)$ for Case 2 or 4 as a function of spacing can be extracted as

$$M_t(g_t) = 1/[f_{res}(g_t)^2 4\pi^2 C_{t1}] - L_{t1}. \quad (5)$$

The dependence of M_t on the space to the maximum extent of $2a_t$ was evaluated with (3) and (5), respectively, at a distance of 5 m by using a commercial loop antenna (ETS-LINDGREN, ETS-6509) and a signal analyzer (Agilent, 35670A) as shown in Fig. 7(b). While M_{t-the} without a gap was 268.0 μH, M_t was 142.5 μH, making the deviation error of 88 %. Obviously, M_t should be modeled from empirical data. From M_t, the coupling coefficient k was extracted to the maximum value of 0.53. In addition, a bandwidth BW
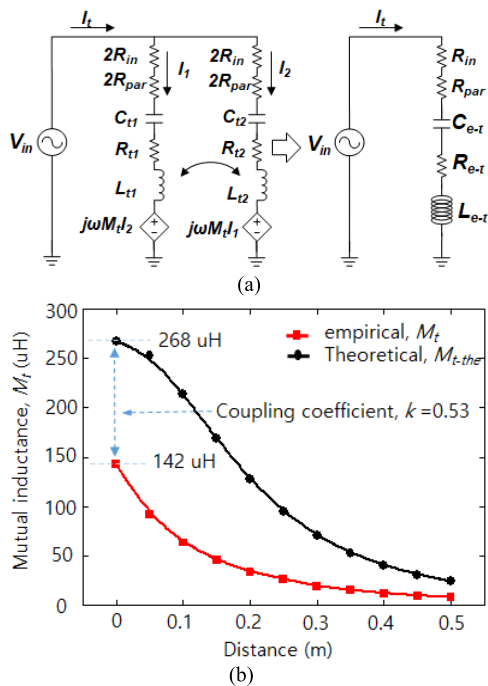

(a)

(b)

FIGURE 7. (a) Electrical circuit for Two loop antennas connected with two Tx drivers and its effective equivalent circuit (b) empirical and theoretical mutual inductances for a Tx module.

and V_{ch} from the Tx system in Case 4 were characterized to optimize the interval of the two coils, as seen in Fig. 8(a). BW was 0.46 kHz at g_t of 0.25 m. When g_t was equal to a_t, the intensity was the maximum. Also, the energy efficiency (V/J) as a figure of merit (FoM) was investigated by using the current probes (TELEDYNE, 2016) of the oscilloscope (TELEDYNE, Surfer 10M). As shown in Fig. 8(b), despite increasing DC current, it saturated at radial distance. Accordingly, the interval of two coils was determined to the radius of the loop antenna, resulting in an optimized scheme: gaped two Tx-gaped two Rx (Case 4).
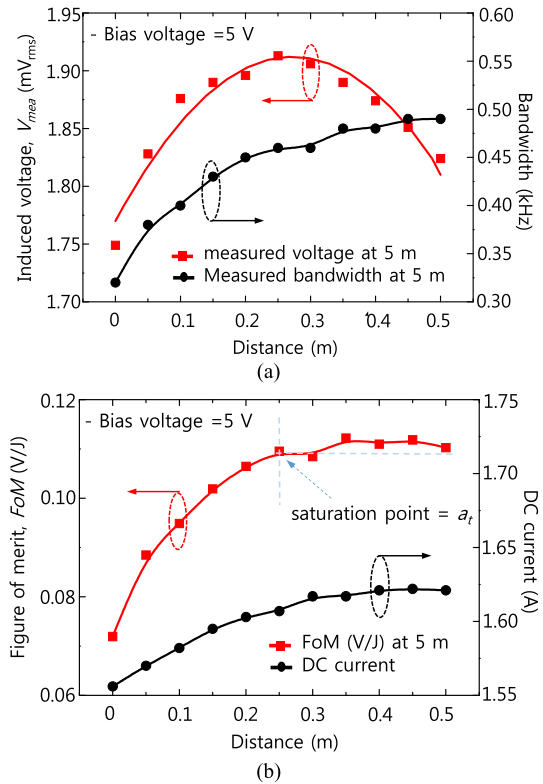

(a)

(b)

FIGURE 8. (a) Induced voltage and Bandwidth characteristics and (b) Figure of merit (FoM) and DC bias current performances for the two loop antennas as a function of distance.

To evaluate whether Case 4 had better output efficiency for Case 1, the power efficiency (mV/W) denoted as the ratio of the induced voltage to the intrinsic Tx power was characterized. At a bias of 5 V, the Tx powers of Case 4 and Case 1 were 2.82 W and 1.41 W, respectively, whereas the voltage intensities were 1.73 mV$_{rms}$ and 0.91 mV$_{rms}$ at the distance of 5 m, respectively. The power efficiency was similar to each other at 0.61 and 0.65, despite an additional 5% loss.

IV. RECEIVING SYSTEM

The design issue of a receiving part is not tangled due to the symmetrical system. The symmetrical correlation makes the design margin of the Rx part much simpler. In this section, we explain the Rx module: the Rx antenna and the

Rx-RM, and conduct electrical modeling based on empirical parameters.

A. TWO OPPOSITELY COUPLING Rx COILS

To explain the effect of two oppositely-coupled inductors from the same voltage source, Fig. 9(a) shows a two mutually coupled inductor circuit that uses dot symbols which define the sign of the mutually induced voltage. Due to the influence of mutual inductance M_r, half of the voltage induced in the gaped two Rx must be less than the magnitude of a single Rx. The KVL equations for the induced voltage V_{ch} are defined as

$$V_{ch} = (R_{r1} + j\omega L_{r1})I_{r1} - j\omega M_r I_{r2} \qquad (6a)$$

$$V_{ch} = j\omega M_r I_{r1} - (R_{r1} + j\omega L_{r1})I_{r2} \qquad (6b)$$

where I_{r1} and I_{r2} are the currents for the two Rx coils. If I_{r1} is equal to I_{r2} under the condition of $d_{ch} \gg g_r$, one terminal voltage V_{r1} is $j\omega(L_{r1} - M_r)I_{r1}$. In the opposite dot symbol, V_{ch} is reduced by the effect of M_r, resulting in the effective self-inductance of $L_{e-r} = L_{r1} - M_r$. If a differential amplifier with two inputs is used in spite of the slight attenuation owing to M_r, V_{ch} is detected almost twice. As a result, V_{ch} can be maximized through Case 4.
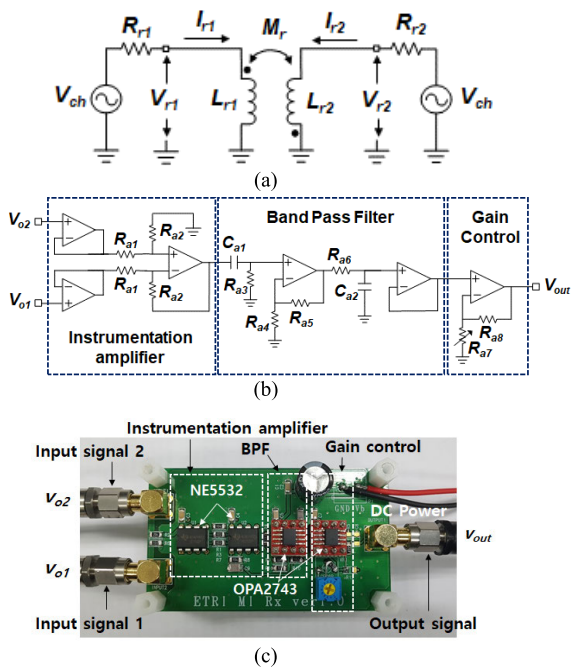

(a)

(b)

(c)

FIGURE 9. (a) Two-coupled inductor circuit using dot symbols (b) the circuit block of the Rx readout module, and (c) the fabricated Rx readout module through the PCB.

B. RX READOUT MODULE AND ITS MODEL

To sense a signal from a gaped two-loop Rx antenna for tiny input signals, an instrumentation amplifier with a customized large voltage gain can be used. It was realized with two commercial operation amplifiers (TI, NE5532) as shown

in Fig. 9(b) where R_{a1} was 1 kΩ, R_{a2} was 100 kΩ. Next, a band pass filter (BPF) was used to shape the input signal using an operation amplifier (TI, OPA2743UA) with the front-end high-pass filter ($C_{a1} = 22$ nF, $R_{a3} = 1$ kΩ) and the rear-end low-pass filter ($R_{a6} = 330$ Ω, $C_{a2} = 15$ nF), where the close loop gain ($R_{a4} = 1$ kΩ and $R_{a5} = 100$ kΩ) from the negative feedback was 100 V/V. The dominant 3-dB high frequency was 7.2 kHz while the dominant 3-dB low frequency was 32.2 kHz. Remarkably, the inserted BPF was not strongly effective due to the high gain configuration of the commercial operation amplifier to detect a mere intensity of signal, which had the gain-bandwidth product of about 10 MHz, showing that the voltage gain around the 1 kHz was the maximum. We added the gain control stage for tuning to the voltage gain A_{gain} of 60 dBV. It was composed of an operation amplifier (TI, OPA2743UA) with a control loop (R_{a8} of 4.7 kΩ and R_{a7} of the varactor of 1 kΩ) to the output terminal of the BPF because the deviation of the characteristic for lumped commercial components exists in practical field. Here, each input impedance R_{pre} of the Rx-RM was 300 kΩ. The fabricated Rx-RM is shown in Fig 9(c).

The equivalent electrical circuit for the Rx-RM is presented to appropriately investigate the Rx module of Case 4, which predicts the channel features reflecting the circumstances. As shown in Fig. 10, each input voltage of the Rx-RM is determined by L_{e-r} with respect to the effect of M_r. If possible, R_{pre} must be high to reduce the signal loss. Although V_{ch} seems to theoretically have a nearly doubled intensity owing to a high R_{pre}, L_{e-r} needs to be determined by empirical data. Due to the opposite connection, each L_{e-r} is featured to have a reduced value by M_r from L_{r1}, which produces much weaker coupling than Case 1. Nevertheless, according to the gaped two-loop Rx scheme, V_{ch} can be made much higher. The V_{ch} of Case 4 is improved by 3 times compared to that of Case 1.
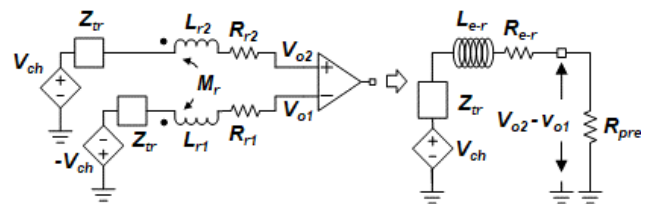

FIGURE 10. Electrical circuit block for Two-loop Rx antennas connected with the Rx-RM and its equivalent circuit.

V. EMPIRICAL EQUIVALENT CIRCUIT MODEL

An equivalent electrical model is useful for intuitive interpretation, since it can predict critical performances, i.e., the Tx power P_t, SNR, received power P_r, and pass loss PL, as well as the magnetic flux density B_{out}. In this section, we discuss the process of modeling and its equivalent circuit, along with the characteristics of a modeled MI channel.

Fig. 11 shows the flow chart for an empirical-based electrical modeling of a MI-based transceiver. Although the model
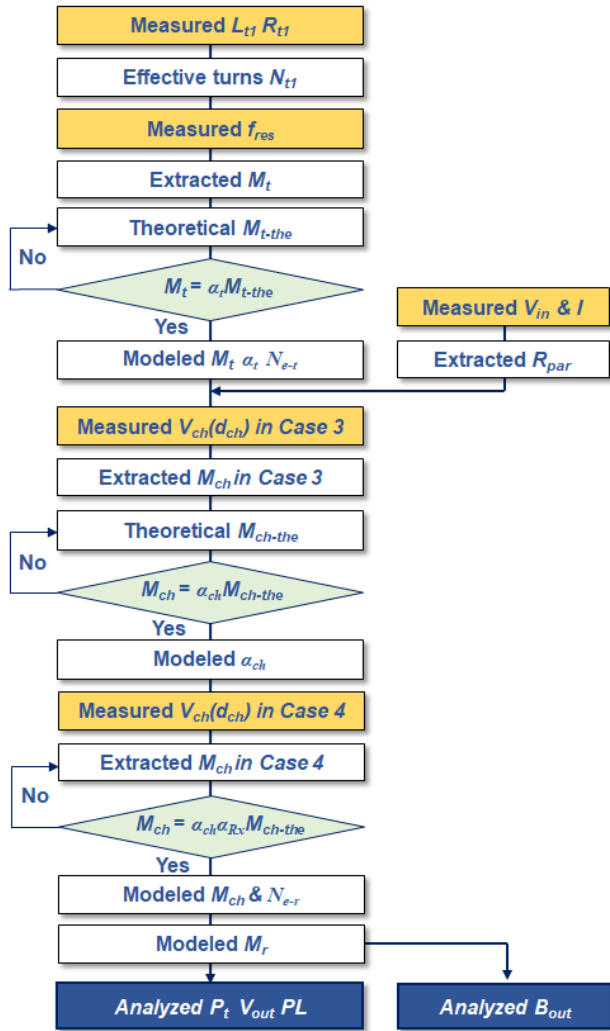
FIGURE 11. Flow chart for modeling the empirical electric circuit of a MI-based RF link system based on gaped two-loop antennas with an interval.

is optimized for Case 4, the process for the other cases can be much simple due to the optional extraction step. Considering the whole process, the model has the following characteristic: it sets the initial data of the theoretical value and determines the correction factor from the measured one. To this end, this model can be easily and accurately applied to practical applications because it can analyze characteristics of the magnetic channel.

As in the flowchart, L_{t1} and R_{t1} are measured first, and the effective number of turns N_{t1} based on the empirical data is determined. Here, N_{t1} is identical to N_{t2}, N_{r1} and N_{r2}. Next, as mentioned in the previous section, M_t is extracted by the measurement of f_{res} as a function of the interval between two coils. For Case 3 and 4, the correction factor a_t and the effective number of turns N_{e-t} are determined from modeled M_t as $M_t = \alpha_t M_{t-the}$. Then, R_{par} is extracted by the measured V_{in} at the output of a Tx driver and measured I_t in Tx coils. This plays a significant role in determining the Tx power. Unlike M_t, M_{ch} and M_r are modeled by V_{ch} at the

Rx point where $V_{ch} = -j\omega M_{ch}I_t$. It is clear that M_{ch} cannot be obtained if I_t in R_{in} and R_{par} is not accurately characterized. M_{ch} reflects the boundary conditions as a specific channel circumstance. For M_{ch}, there are two correction factors α_{ch} and α_{Rx}, where α_{ch} is about to the magnetic channel effect and α_{Rx} is related with an Rx scheme itself. For Case 4, M_{ch} is to be $\alpha_{ch}\alpha_{Rx}M_{ch-the} \approx \alpha_{ch}\alpha_{Rx}\mu_0\pi N_{e-t}N_{e-r}(a_t^2 a_r^2/2d_{ch}^3)$ under the conditions of $d_{ch} \gg a_r$, where N_{e-r} is the effective number of turns for the Rx part. α_{ch} for Case 4 should be extracted by Case 3 due to one Rx coil with no effect of M_r. Obviously, α_{ch} is a critical factor showing magnetic field channel characteristics containing all of the actual surrounding environment. α_{Rx} is a correction factor related only to Case 4, which is set to 2 for Case 4. After extracting α_{ch} by Case 3, N_{e-r} is modeled from V_{ch} of Case 4. Then, M_r is modeled from $L_{r1} - L_{e-r}$ where L_{e-r} is $\mu_0\pi(N_{e-r})^2 a_r/2$. N_{e-r} is less than N_{r1} due to the effect of M_r. The fundamental process of modeling is completed by extracting M_r. After that, characterization of the MI transceiver is carried out using this model, leading to P_t, P_r, SNR, PL and B_{out}.

Fig. 12 shows an empirical-based equivalent circuit model applicable in all cases mentioned in the previous section. This is possible because the circuit is applied to both the Tx and Rx modules. Since the model has a signal source including R_{in} as the Thevenin's equivalent circuit as well as R_{par}, it can evaluate accurately the performance. The voltage gain is determined by

$$\frac{V_{out}(\omega)}{V_{in}(\omega)} = \left(\frac{Z_{t-ant} + Z_{rt}}{Z_{t-tot} + Z_{rt}}\right)\left(\frac{-j\omega M_{ch}}{Z_{t-tot}}\right)\left(\frac{R_{pre}}{Z_{tr} + Z_r + R_{pre}}\right)$$
$$\times A_{gain}\left(\frac{R_{load}}{R_{mod} + R_{load}}\right) \quad (7)$$

where $Z_{t-tot} = R_{in} + R_{par} + R_{e-t} + j\omega L_{e-t} + 1/j\omega C_{e-t}$, $Z_{t-ant} = R_{e-t} + j\omega L_{e-t} + 1/j\omega C_{e-t}$, $Z_{rt} = \omega^2 M_{ch}^2/(Z_r + R_{pre})$, $Z_{tr} = \omega^2 M_{ch}^2/Z_{t-tot}$, $Z_r = R_{e-r} + j\omega L_{e-r}$, $A_{gain} = V_{mod}/(V_{o2} - V_{o1})$. Also, R_{mod} is the output impedance of Rx-RM and R_{load} is the load resistance. Since SNR is proportional to M_{ch}, the parameters of M_{ch}, especially a_r, can be tuned to improve channel performance. In addition, from α_{ch}, the channel influence is confirmed as much as the difference to the theoretical value M_{ch-the}.

VI. PERFORMANCE EVALUATION

We perform whether a MI-based hardware system could be used in buildings with concrete walls as well as an underground hallway. The four cases were analyzed and compared with each other, where all the loop antennas had the 0.25 m radius and the effective 23.3 turns. The Tx power was characterized first in the semi-anechoic chamber, and then compared with values evaluated in an underground corridor. Actually, V_{ch} was compared through magnetic channels between the floors of a real building.

A. MI OPERATION PRINCIPLES

Fig. 13 shows figures of the experimental set up for Case 4 in a semi-anechoic chamber. Measured I_1 and I_2 at 20.84 kHz
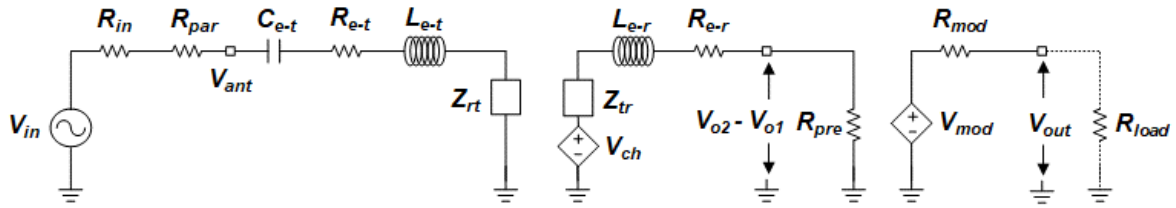
FIGURE 12. Empirical electrical circuit consisting of three parts (the Tx, the magnetic channel, and the Rx parts) of a MI-based RF link system based on symmetrical two loop antennas with an interval.
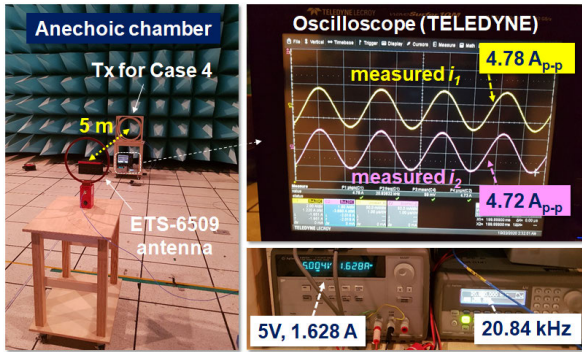

FIGURE 13. Experimental set-up evaluating the Tx characteristics of Case 4 at a distance of 5 m in a semi-anechoic chamber.
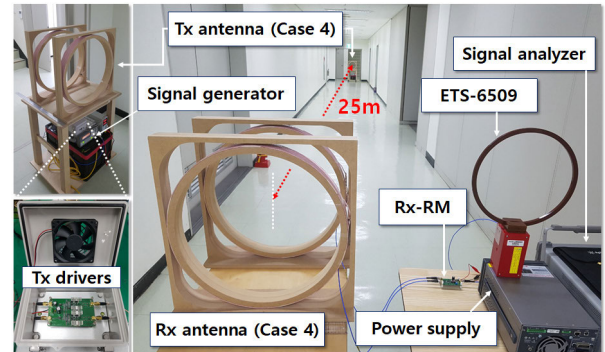

FIGURE 14. Experimental set-up evaluating the Tx-Rx characteristics of Case 4 at a distance of 25 m in a real underground corridor.

were 2.39 A and 2.36 A, respectively, at DC power of 8.14 W in the distance of 5 m. The current of Case 1 was 2.42 A at DC power of 4.2 W. Here, V_{in} and $2R_{in}$ for each Tx driver were 1.342 V_{rms} and 21 mΩ at 5 V, respectively. R_{par} was extracted to 139.5 mΩ from I, V_{in}, R_{in}, R_{ant} and R_{par}. V_{ch} was detected by both ETS-6509 with an antenna factor of 18.4 S/m at an operating frequency and a signal analyzer with an input impedance of 1 MΩ. It was determined to 0.87 mV$_{rms}$ from the half value of the measured voltage with the interval of 5 m in the semi-anechoic chamber. It means a magnetic field at the point to be 15.9 mA/m. Also, the magnetic channel influence in an underground hallway was evaluated as shown in Fig. 14. The line of sight was aligned to each center between the Tx and the Rx antennas up to the interval range of 25 m which was a hundred times the radius of the antenna. V_{ch} between the Tx and the Rx with the interval of 5 m was 0.66 mV$_{rms}$ related to a magnetic field of 12.1 mA/m whereas V_{ch} in the semi-anechoic chamber was 0.87 mV$_{rms}$. Obviously, surrounding environment made the difference by 0.21 mV$_{rms}$ from the reference condition on 0.87 mV$_{rms}$, compared with that of the semi-anechoic chamber.

As shown in Fig. 15(a), the V_{ch} was compared in different cases at d_{ch} of 25 m. V_{ch} at Case 1 was 40.5 μV$_{rms}$ at the Tx power of 31.5 dBm. Here, on the signal analyzer's two-channel output, the top of ETS-6509 and the bottom of Case 1 represented 8.1 μV$_{rms}$ and 40.5 μV$_{rms}$, respectively. V_{ch} for ETS-6509 was half of the initial value, leading to 4.05 μV$_{rms}$. From the antenna factor of 18.4 S/m for ETS-6509, that of Case 1 was extracted to be 1.84 S/m, which

represented a magnetic field through V_{ch}. The magnetic field for Case 1 was 104 μA/m at 31.5 dBm. For Case 3, V_{ch} was 75.0 μV$_{rms}$ at 34.5 dBm, as shown in Fig. 15(b). It is clear that V_{ch} was not 81.0 μV$_{rms}$, which was twice 40.5 μV$_{rms}$, but 75.0 μV$_{rms}$ due to the influence of M_t. The magnetic field and M_{ch} for Case 3 were 195 μA/m and 171 pH, respectively, at 34.5 dBm. Here, α_{ch} was modeled to 0.86. It proved that V_{ch} was reduced by 14% in the underground corridor compared to the free space. Fig. 15(c) demonstrates the validity of the Rx-RM because V_{ch} of the same system in Fig. 15(b) was amplified by 60 dBV to 75.9 mV$_{rms}$. Conversely, for Case 2, V_{ch} was enhanced 1.67 times from Case 1, as shown in Fig. 15(d). Fig. 15(e) and 15(f) have the same structure except for the interval of the antenna's radius. As expected, owing to M_r, V_{ch} for the two Rx coils with no gap was 13.6% lower than that of Case 4. M_{ch} was 274 pH at 34.5 dBm. N_{e-r} was extracted to 18.7, which determined M_r to be 96 μH. M_r in Case 4 was 1.5 times higher than Case 1.

Fig. 16(a) shows the performances of M_{ch} up to the distance of 25 m. The measured and modeled M_{ch} at 25 m were 276 pH and 274 pH, respectively, with little difference at the operating frequency of 20.84 kHz. Thus, the slight difference value validates the empirical electrical model. As seen in Fig. 16(b), V_{ch} for Case 4 was 171 μV$_p$ (121.0 μV$_{rms}$) in a 25 m at the resonant frequency, giving almost the same result as measured in Fig. 15(f). Case 4 had three times higher voltage than Case 1, which was equal to the SNR of 9.5 dB. If R_{pre} was replaced to 50 Ω, P_r could be modeled. P_r for Case 4 was -66.2 dBm while P_r for Case 4 was -76.6 dBm, marking the
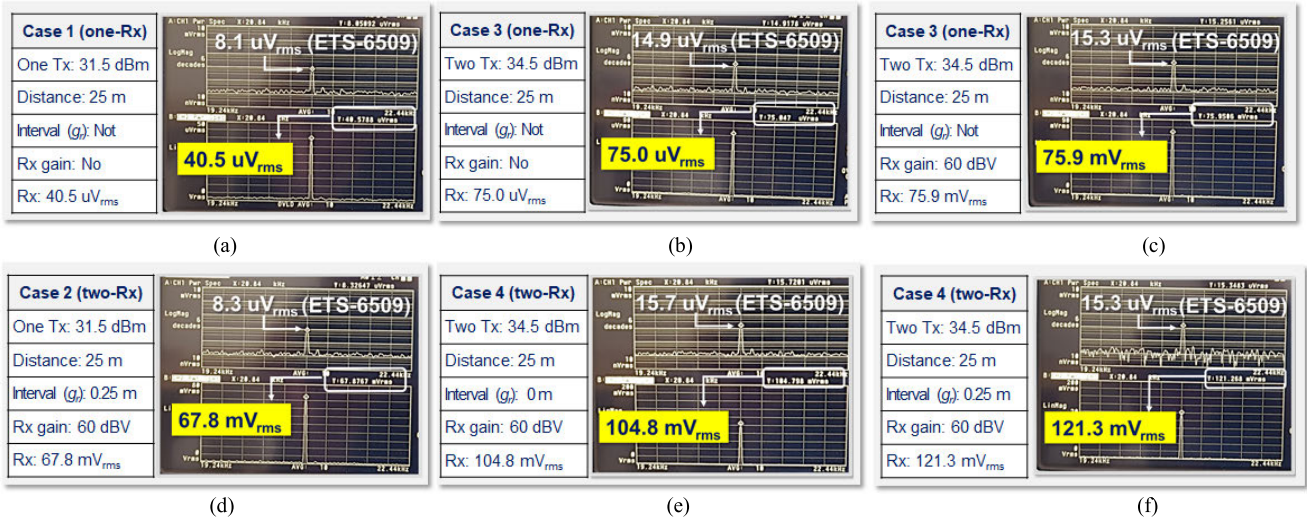
FIGURE 15. Induced voltage of (a) Case 1, (b) Case 3, (c) Case 3 through the Rx-RM, (d) Case 2 through the Rx-RM, (e) Case 4 with no interval through the Rx-RM, (f) Case 4 with an interval through the Rx-RM at a distance of 25 m in a real underground corridor.
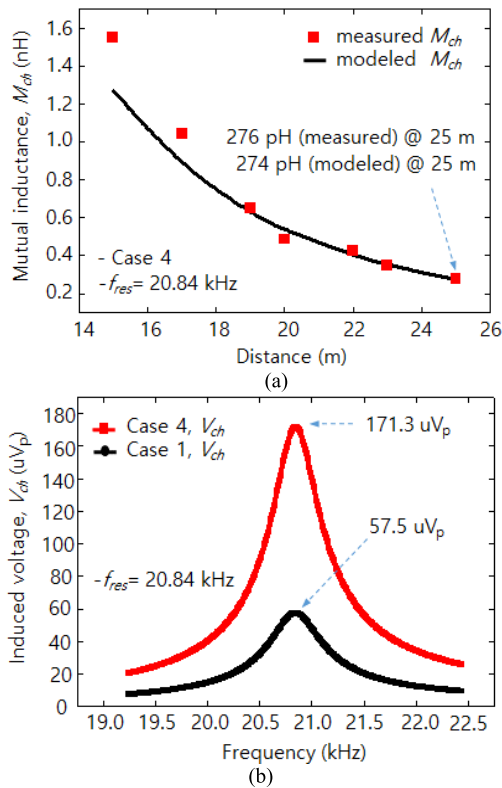

FIGURE 16. (a) Measured and modeled performances of M_{ch} for Case 4 as a function of distance and comparison of modeled (b) V_{ch} for Case 1 and Case 4 in an underground corridor as a function of frequency.

improvement of 10.4 dB. From the circuit, V_{ch} was modeled up to the range of 100 m, as shown in Fig. 17(a). When the noise baseline in the 3.2 kHz span was $2 \mu V_{rms}$, the maximum distance in Case 4 within an SNR of 9.5 dB was 44.6 % longer than Case 1. Accordingly, the magnetic flux density B_{out} was

modeled because B_{out} was considered as a performance index for a sensor node in MI-based communication. Fig. 17(b) shows the results. Case 4 at 34.5 dBm is capable of forming B_{out} of 3.8 pT at a distance of 100 m. Moreover, according to the 10 pT requirement, Case 4 can cover a range of up to 72.3 m. The characteristics of a magnetic field channel can be evaluated by PL. Fig. 18 presents P_r and path loss PL of Case 1 and Case 4 as a function of distance. At 100 m, P_r of Case 4 was -102.1 dBm and P_r of Case 1 was -112.7 dBm. The PL is described by the proposed model as

$$\frac{P_r(d_{ch})}{P_t(0)} = \frac{|V_{ch}|^2}{2|Z_{tr}+Z_r+R_{pre}|^2} Re\{R_{pre}\} \Bigg/ \frac{|V_{in}|^2}{2|Z_{t-tot}+Z_{rt}|^2} \times Re\{Z_{t-ant}+Z_{rt}\}. \quad (8)$$

For Case 4, PLs at 25 m and 100 m distance were 100.7 dB and 136.6 dB, respectively, whereas for Case 1, PLs at 25 m and 100 m distance were 108.1 dB and 144.2 dB, respectively. Here, the decay trend for the two systems was similar even as the distance increases.

B. INTER-LAYERS IN A BUILDING

We evaluate whether a MI-based link system could be used in buildings with concrete walls due to practical necessity. Fig. 19(a) describes a diagram for evaluating the MI channel effect in a real building environment. V_{ch} was investigated according to the floor spacing. There was no significant reduction in V_{ch} in the single-floor spacing compared to the line-of-sight distance, but V_{ch} reduced considerably in the two-layer interval. The measured data in the single-floor spacing is presented in Fig. 19(b). The induced voltage V_1 of ETS-6509 at 34.5 dBm had 327 uVrms. For Case 4, V_{ch} was saturated to 1.75 Vrms due to the high gain of the Rx-RM, showing that the single-story concrete floor had little effect on the channel medium. However, it was confirmed
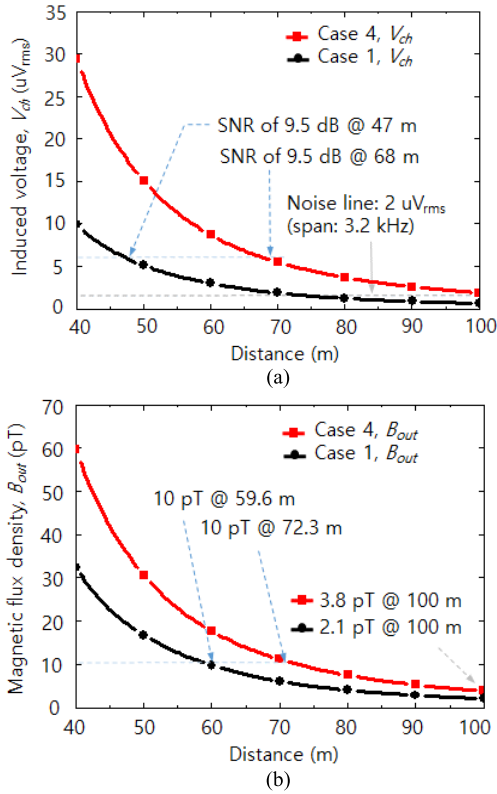
FIGURE 17. Comparison of modeled (a) V_{ch} and (b) B_{out} for Case 1 and Case 4 under the condition of an underground corridor as a function of distance.
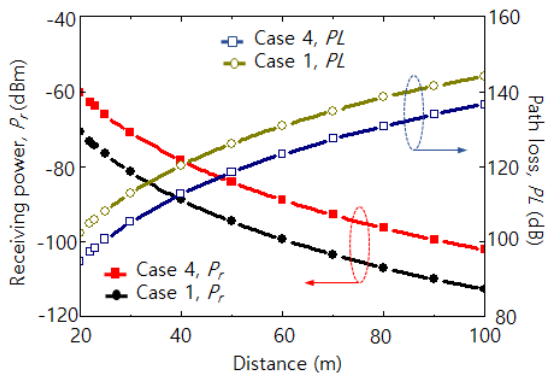

FIGURE 18. Comparisons of modeled P_r and PL for Case 1 and Case 4 under the condition of an underground corridor as a function of distance.

FIGURE 19. (a) Diagram for evaluating the MI channel effect in a real building environment and measured V_{ch} for Case 4 (b) in the single-floor spacing and (c) between the second and basement floors.

TABLE 1. Characteristics and performances for case 4.

Meaning	Value
V_{ch} in a 25 m corridor at 34.5 dBm Tx	121.3 µV$_{rms}$
SNR through the Rx-RM on the V_{ch}	46 dB
P_r in a 25 m corridor at 34.5 dBm Tx (R_{pre}= 50 Ω)	239 pW
PL in a 25 m corridor for the P_r	100.7 dB
Distance for 9.5 dB SNR at 34.5 dBm Tx (modeled)	68.0 m
Distance for 10 pT at 34.5 dBm Tx (modeled)	72.3 m
B_{out} in a 100 m corridor at 34.5 dBm Tx (modeled)	3.8 pT
PL in a 100 m corridor at 34.5 dBm Tx (modeled)	136.6 dB
SNR in two-story spacing at 34.5 dBm Tx	8.7 dB

that the two floors of concrete deteriorated V_{ch} tremendously. Fig. 19(c) shows V_{ch} between the second and basement floors of the building. At 34.5 dBm, the measured voltage V_2 was 19.1 mV$_{rms}$ leading to SNR of 8.7 dB which was considered to a magnetic channel influence in the underground corridor of 70 m. Also, V_1 of ETS-6509 was to be 2.24 µV$_{rms}$ with the noise baseline of 1 µV$_{rms}$ in the span of 3.2 kHz. The characterisitics and performances for Case 4 was listed in Table 1, where f_{req} was 20.84 kHz. As a result, these data indicated that the MI-based transceiver could be implemented through interlays on the second floor or higher of the building
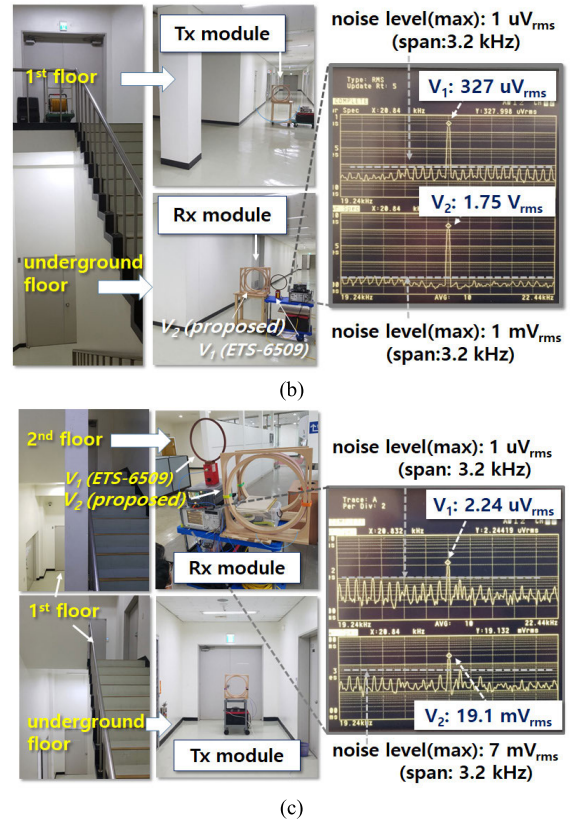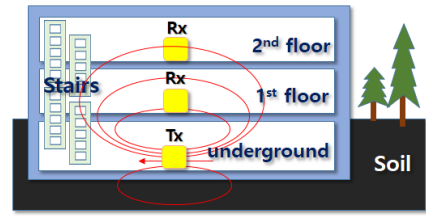
only under high Tx power conditions of 34.5 dBm or higher. Table 2 shows the comparison results and characteristics of the existing technology for the MI-based sensor node. In the MI communication [10], [15], the connection technology of the sensor node is explained based on the technology using COTS products in the MHz band. On the other hand, in the

TABLE 2. Comparison results and characteristics of the existing technology for the MI-based sensor nodes.

Tx -Rx Structure	1-1 circular [15]	multi-multi [10]	3-3 cubic [8]	3-3 sphere [2]	This work (Case 4)
Coil size(max) (L: length/r: radius)	66 mm (L)	40 mm (r)	300 mm (L)	104 mm (r)	250 mm (r)
Tx/Rx part	COTS 13.56 MHz,18mA 60% (PDP) @ 12 m	42 turns f_0 =50 MHz, 1 A -62 dB @ 2 m	80 turns f_0 = 2.025 kHz Magnetic vector modulation (80 bps)	COTS, 29 turns 125 kHz, 0.8 A 1 kbps 80 μV (sensitivity)	17 turns 20.84 kHz, 34.5 dBm 239 pW @ 25 m
Range	12 m (indoor)	20 m	35 m	38 m	25 m (two floors)
Model	FEM (theoretical)	FEM (theoretical)	Measurement	Circuit (theoretical)	Circuit (empirical)
Application	Test-bed	Complex	Underground	Complex	Underground

application field of MI localization [2], [8], the detection method through the WUSNs based on the low-frequency 3-D antenna structure is described. Our technology (Case 4) confirmed the signal connection (SNR: 8.7 dB) with the low Tx power (34.5 dBm) at the interval of the second floor in the building. The summary of the contents developed through this paper is as follows.

1. A low-power, low-volume MI hardware platform, which maximized SNR for two-way connectivity, has been developed as the physical layer of WUSNs.
2. Since an empirical circuit model completely consisting of variables from the signal source to the output load has been developed, the characteristics of the real environment reflecting a magnetic channel were evaluated.
3. The MI-based transceiver has been deployed in a building with concrete walls (two-story space) in order to test and analyze the feasibility of the proposed hardware.

VII. CONCLUSION

This paper introduced a low-power, low-frequency MI-based transceiver that could be used in underground environments blocked by stairs or floors. In addition, we performed electrical modeling using empirical-based variables to reflect the boundary conditions of a real environment. Obviously, we found that signal attenuation occurs sharply when we measured between two layers rather than between one layer. Likewise, when there were barrier walls in the basement rather than the open corridor space, the signal also rapidly decreased. The results show that MI-based data link over certain intervals (e.g., 25 m or more) can be performed only when the Tx power level is generally above 30 dBm. Hence, our study confirmed that the proposed mobile low-frequency MI hardware system is suitable for extreme or emergency two-way communications in blocked underground environments.

REFERENCES

[1] Y.-W. Kuo, C.-L. Li, J.-H. Jhang, and S. Lin, "Design of a wireless sensor network-based IoT platform for wide area and heterogeneous applications," *IEEE Sensors J.*, vol. 18, no. 12, pp. 5187–5197, May 2018, doi: 10.1109/JSEN.2018.2832664.

[2] N. Ahmed, A. Radchenko, D. Pommerenke, and Y. R. Zheng, "Design and evaluation of low-cost and energy-efficient magneto-inductive sensor nodes for wireless sensor networks," *IEEE Syst. J.*, vol. 13, no. 2, pp. 1135–1144, Jun. 2019, doi: 10.1109/JSYST.2018.2841872.

[3] A. Pal and K. Kant, "NFMI: Near field magnetic induction based communication," *Comput. Netw.*, vol. 181, Nov. 2020, Art. no. 107548, doi: 10.1016/j.comnet.2020.107548.

[4] Z. Sun and I. F. Akyildiz, "Magnetic induction communications for wireless underground sensor networks," *IEEE Trans. Antennas Propag.*, vol. 58, no. 7, pp. 443–482, Apr. 2010, doi: 10.1002/9780470515181.ch17.

[5] T. E. Abrudan, O. Kypris, N. Trigoni, and A. Markham, "Impact of rocks and minerals on underground magneto-inductive communication and localization," *IEEE Access*, vol. 4, pp. 3999–4010, 2016, doi: 10.1109/ACCESS.2016.2597641.

[6] I. F. Akyildiz and E. P. Stuntebeck, "Wireless underground sensor networks: Research challenges," *Ad Hoc Netw.*, vol. 4, no. 6, pp. 669–686, Nov. 2006, doi: 10.1016/j.adhoc.2006.04.003.

[7] S. Yarkan, S. Guzelgoz, H. Arslan, and R. R. Murphy, "Underground mine communications: A survey," *IEEE Commun. Surveys Tuts.*, vol. 11, no. 3, pp. 125–142, 3rd Quart., 2009, doi: 10.1109/SURV.2009.090309.

[8] A. Markham and N. Trigoni, "Magneto-inductive networked rescue system (MINERS): Taking sensor networks underground," in *Proc. 11th Int. Conf. Inf. Process. Sensor Netw. (IPSN)*, 2012, pp. 317–327, doi: 10.1145/2185677.2185746.

[9] H. Guo, Z. Sun, J. Sun, and N. M. Litchinitser, "M²I: Channel modeling for metamaterial-enhanced magnetic induction communications," *IEEE Trans. Antennas Propag.*, vol. 63, no. 11, pp. 5072–5087, Nov. 2015, doi: 10.1109/TAP.2015.2480095.

[10] H. Guo, Z. Sun, and C. Zhou, "Practical design and implementation of metamaterial-enhanced magnetic induction communication," *IEEE Access*, vol. 5, pp. 17213–17229, 2017, doi: 10.1109/ACCESS.2017.2719406.

[11] B. Gulbahar and O. B. Akan, "A communication theoretical modeling and analysis of underwater magneto-inductive wireless channels," *IEEE Trans. Wireless Commun.*, vol. 11, no. 9, pp. 3326–3334, Sep. 2012, doi: 10.1109/TWC.2012.070912.111943.

[12] H. Guo, Z. Sun, and P. Wang, "Channel modeling of MI underwater communication using tri-directional coil antenna," in *Proc. IEEE Global Commun. Conf. (GLOBECOM)*, Dec. 2015, pp. 1–6, doi: 10.1109/GLOCOM.2015.7417399.

[13] Z. Zheng, Y. Fu, K. Liu, R. Xiao, X. Wang, and H. Shi, "Three-stage vertical distribution of seawater conductivity," *Sci. Rep.*, vol. 8, no. 1, pp. 1–10, Dec. 2018, doi: 10.1038/s41598-018-27931-y.

[14] A. R. Silva and M. Moghaddam, "Operating frequency selection for low-power magnetic induction-based wireless underground sensor networks," in *Proc. IEEE Sensors Appl. Symp. (SAS)*, Apr. 2015, pp. 1–6, doi: 10.1109/SAS.2015.7133600.

[15] R. K. Gulati, A. Pal, and K. Kant, "Experimental evaluation of a near-field magnetic induction based communication system," in *Proc. IEEE Wireless Commun. Netw. Conf. (WCNC)*, Apr. 2019, pp. 1–6, doi: 10.1109/WCNC.2019.8885541.

[16] J.-Y. Kim, I.-K. Cho, H. J. Lee, J. Lee, J.-I. Moon, S.-M. Kim, S.-W. Kim, S. Ahn, and K. Kim, "A novel experimental approach to the applicability of high-sensitivity giant magneto-impedance sensors in magnetic field communication," *IEEE Access*, vol. 8, pp. 193091–193101, 2020, doi: 10.1109/ACCESS.2020.3032702.

[17] S. Kisseleff, I. F. Akyildiz, and W. H. Gerstacker, "Throughput of the magnetic induction based wireless underground sensor networks: Key optimization techniques," *IEEE Trans. Commun.*, vol. 62, no. 12, pp. 4426–4439, Dec. 2014, doi: 10.1109/TCOMM.2014.2367030.

[18] S.-C. Lin, I. F. Akyildiz, P. Wang, and Z. Sun, "Distributed cross-layer protocol design for magnetic induction communication in wireless underground sensor networks," *IEEE Trans. Wireless Commun.*, vol. 14, no. 7, pp. 4006–4019, Jul. 2015, doi: 10.1109/TWC.2015.2415812.

[19] I. F. Xin, A. Tan, and Z. Sun, "Wireless underground sensor networks," *IEEE Antennas Propag. Mag.*, vol. 57, no. 4, pp. 74–87, 2015, doi: 10.1201/b17224-24.

[20] T. E. Abrudan, Z. Xiao, A. Markham, and N. Trigoni, "Underground incrementally deployed magneto-inductive 3-D positioning network," *IEEE Trans. Geosci. Remote Sens.*, vol. 54, no. 8, pp. 4376–4391, Aug. 2016, doi: 10.1109/TGRS.2016.2540722.

[21] X. Tan, Z. Sun, P. Wang, and Y. Sun, "Environment-aware localization for wireless sensor networks using magnetic induction," *Ad Hoc Netw.*, vol. 98, Mar. 2020, Art. no. 102030, doi: 10.1016/j.adhoc.2019.102030.

HYUN JOON LEE received the B.S., M.S., and Ph.D. degrees from the Department of Physics, Pusan National University, Busan, South Korea, in 2008, 2011, and 2018, respectively.

From 2018 to 2019, he was a Postdoctoral Associate with the Korea Research Institute of Standards and Science, working on optical magnetometry. Since 2019, he has been with the Electronics and Telecommunications Research Institute, Daejeon, South Korea. His research interests include ultra-low field magnetic resonance and the development of highly sensitive quantum sensors.

JANG-YEOL KIM received the B.S. and M.S. degrees in information and communication engineering from Chungbuk National University, Cheongju, South Korea, in 2010 and 2012, respectively, and the Ph.D. degree in information and communication engineering from Chungbuk National University, Cheongju, South Korea, in 2017.

Since 2012, he has been with the Electronics Telecommunications Research Institute, Daejeon, South Korea. His research interests include antenna design, thermal therapy algorithms, microwave sensing, and electromagnetic sensor.

JAEWOO LEE received the B.S. degree in electrical and electronics engineering from Korea University, Seoul, South Korea, in 2000, the M.S. degree in information and communication engineering from the Gwangju Institute of Science and Technology, Gwangju, South Korea, in 2002, and the Ph.D. degree in electrical engineering from the Korea Advanced Institute of Science and Technology, Daejeon, South Korea, in 2017.

Since 2002, he has been with the Electronics and Telecommunication Research Institute, Daejeon, working in the field of RF devices, sensors using full-CMOS/MEMS processes, thermoelectric modules. His current research interest includes the development of sensor nodes for wireless communication applications.

IN-KUI CHO received the B.S. and M.S. degrees from the Department of Electronic Engineering, Kyungpook National University, Daegu, South Korea, in 1997 and 1999, respectively, and the Ph.D. degree in electrical engineering from the Korea Advanced Institute of Science and Technology, Daejeon, South Korea, in 2007.

Since May 1999, he has been with the Electronics and Telecommunications Research Institute, Daejeon, where he has designed and developed optical backplane, optical chip-to-chip interconnect system, and magnetic resonance wireless power transfer. His current research interests include simulation and development of WPT components, such as planar magnetic resonator and magnetic resonator for three dimensional WPT.

• • •